

# Flat super-oscillatory lens for heat-assisted magnetic recording with sub-50nm resolution

Guanghui Yuan,<sup>1</sup> Edward T. F. Rogers,<sup>2</sup> Tapashree Roy,<sup>2</sup> Zexiang Shen,<sup>1</sup>  
and Nikolay I. Zheludev<sup>1,2,\*</sup>

<sup>1</sup>Centre for Disruptive Photonic Technologies, Nanyang Technological University, Singapore 637371, Singapore  
<sup>2</sup>Optoelectronics Research Centre and Centre for Photonic Metamaterials, University of Southampton, Southampton, UK

\*nzheludev@ntu.edu.sg

**Abstract:** Heat-assisted magnetic recording (HAMR) is a future roadmap technology to overcome the superparamagnetic limit in high density magnetic recording. Existing HAMR schemes depend on a simultaneous magnetic stimulation and light-induced local heating of the information carrier. To achieve high-density recorded data, near-field plasmonic transducers have been proposed as light concentrators. Here we suggest and investigate in detail an alternative approach exploiting a far-field focusing device that can focus light into sub-50nm hot-spots in the magnetic recording layer using a laser source operating at 473nm. It is based on a recently introduced super-oscillatory flat lens improved with the use of solid immersion, giving an effective numerical aperture as high as 4.17. The proposed solution is robust and easy to integrate with the magnetic recording head thus offering a competitive advantage over plasmonic technology.

©2014 Optical Society of America

**OCIS codes:** (100.6640) Superresolution; (050.1965) Diffractive lenses; (050.1380) Binary optics; (210.4590) Optical disks.

---

## References and links

1. B. C. Stipe, T. C. Strand, C. C. Poon, H. Balamane, T. D. Boone, J. A. Katine, J.-L. Li, V. Rawat, H. Nemoto, A. Hirotsune, O. Hellwig, R. Ruiz, E. Dobisz, D. S. Kercher, N. Robertson, T. R. Albrecht, and B. D. Terris, "Magnetic recording at 1.5 Pb m<sup>-2</sup> using an integrated plasmonic antenna," *Nat. Photonics* **4**(7), 484–488 (2010).
2. M. H. Kryder, E. C. Gage, T. W. McDaniel, W. A. Challener, R. E. Rottmayer, G. P. Ju, Y.-T. Hsia, and M. F. Erden, "Heat-assisted magnetic recording," *Proc. IEEE* **96**(11), 1810–1835 (2008).
3. W. A. Challener, C. B. Peng, A. V. Itagi, D. Karns, W. Peng, Y. G. Peng, X. M. Yang, X. B. Zhu, N. J. Gokemeijer, Y.-T. Hsia, G. Ju, R. E. Rottmayer, M. A. Seigler, and E. C. Gage, "Heat-assisted magnetic recording by a near-field transducer with efficient optical energy transfer," *Nat. Photonics* **3**(4), 220–224 (2009).
4. P. N. Minh, T. Ono, and M. Esashi, "High throughput aperture near-field scanning optical microscopy," *Rev. Sci. Instrum.* **71**(8), 3111–3117 (2000).
5. X. Zhang and Z. W. Liu, "Superlenses to overcome the diffraction limit," *Nat. Mater.* **7**(6), 435–441 (2008).
6. N. Fang, H. Lee, C. Sun, and X. Zhang, "Sub-diffraction-limited optical imaging with a silver superlens," *Science* **308**(5721), 534–537 (2005).
7. J. Rho, Z. L. Ye, Y. Xiong, X. B. Yin, Z. W. Liu, H. Choi, G. Bartal, and X. Zhang, "Spherical hyperlens for two-dimensional sub-diffractive imaging at visible frequencies," *Nat. Commun.* **1**(9), 143 (2010).
8. J. Y. Lee, B. H. Hong, W. Y. Kim, S. K. Min, Y. Kim, M. V. Jouravlev, R. Bose, K. S. Kim, I. C. Hwang, L. J. Kaufman, C. W. Wong, P. Kim, and K. S. Kim, "Near-field focusing and magnification through self-assembled nanoscale spherical lenses," *Nature* **460**(7254), 498–501 (2009).
9. Z. B. Wang, W. Guo, L. Li, B. Luk'yanchuk, A. Khan, Z. Liu, Z. C. Chen, and M. H. Hong, "Optical virtual imaging at 50 nm lateral resolution with a white-light nanoscope," *Nat. Commun.* **2**, 218 (2011).
10. F. M. Huang, T. S. Kao, V. A. Fedotov, Y. F. Chen, and N. I. Zheludev, "Nanohole array as a lens," *Nano Lett.* **8**(8), 2469–2472 (2008).
11. T. Roy, E. T. F. Rogers, and N. I. Zheludev, "Sub-wavelength focusing meta-lens," *Opt. Express* **21**(6), 7577–7582 (2013).
12. E. T. F. Rogers, S. Savo, J. Lindberg, T. Roy, M. R. Dennis, and N. I. Zheludev, "Super-oscillatory optical needle," *Appl. Phys. Lett.* **102**(3), 031108 (2013).

13. E. T. F. Rogers, J. Lindberg, T. Roy, S. Savo, J. E. Chad, M. R. Dennis, and N. I. Zheludev, "A super-oscillatory lens optical microscope for subwavelength imaging," *Nat. Mater.* **11**(5), 432–435 (2012).
14. E. Greenfield, R. Schley, I. Hurwitz, J. Nemirovsky, K. G. Makris, and M. Segev, "Experimental generation of arbitrarily shaped diffractionless superoscillatory optical beams," *Opt. Express* **21**(11), 13425–13435 (2013).
15. S. M. Mansfield and G. S. Kino, "Solid immersion microscope," *Appl. Phys. Lett.* **57**(24), 2615 (1990).
16. M. V. Berry and S. Popescu, "Evolution of quantum superoscillations and optical superresolution without evanescent waves," *J. Phys. Math. Gen.* **39**(22), 6965–6977 (2006).
17. F. M. Huang, Y. Chen, F. J. Garcia de Abajo, and N. I. Zheludev, "Optical super-resolution through super-oscillations," *J. Opt. A, Pure Appl. Opt.* **9**(9), S285–S288 (2007).
18. F. M. Huang, N. Zheludev, Y. Chen, and F. J. Garcia de Abajo, "Focusing of light by a nanohole array," *Appl. Phys. Lett.* **90**(9), 091119 (2007).
19. N. I. Zheludev, "What diffraction limit?" *Nat. Mater.* **7**(6), 420–422 (2008).
20. E. T. F. Rogers and N. I. Zheludev, "Optical super-oscillations: sub-wavelength light focusing and super-resolution imaging," *J. Opt.* **15**(9), 094008 (2013).
21. E. T. F. Rogers, N. I. Zheludev, V. Savinov, T. Roy, S. Savo, M. R. Dennis, and J. Lindberg, "Superoscillatory lens device," GB patent application number GB1201936.0 and PCT patent application number PCT/GB2013/050114 (2012).
22. A. M. H. Wong and G. V. Eleftheriades, "An optical super-microscope for far-field, real-time imaging beyond the diffraction limit," *Sci. Rep.* **3**, 1715 (2013).
23. D. Ganic, X. S. Gan, and M. Gu, "Focusing of doughnut laser beams by a high numerical-aperture objective in free space," *Opt. Express* **11**(21), 2747–2752 (2003).
24. M. Mansuripur, "Distribution of light at and near the focus of high-numerical-aperture objectives," *J. Opt. Soc. Am. A* **3**(12), 2086–2093 (1986).
25. M. Mansuripur, "Certain computational aspects of vector diffraction problems," *J. Opt. Soc. Am. A* **6**(6), 786–805 (1989).
26. V. V. Kotlyar and A. A. Kovalev, "Nonparaxial propagation of a Gaussian optical vortex with initial radial polarization," *J. Opt. Soc. Am. A* **27**(3), 372–380 (2010).
27. H. P. Ye, C. W. Qiu, K. Huang, J. H. Teng, B. Luk'yanchuk, and S. P. Yeo, "Creation of a longitudinally polarized subwavelength hotspot with an ultra-thin planar lens: vectorial Rayleigh-Sommerfeld method," *Laser Phys. Lett.* **10**(6), 065004 (2013).
28. T. Liu, J. B. Tan, J. Liu, and H. T. Wang, "Vectorial design of super-oscillatory lens," *Opt. Express* **21**(13), 15090–15101 (2013).
29. N. Jin and Y. Rahmat-Samii, "Advances in particle swarm optimization for antenna designs: Real-number, binary, single-objective and multiobjective implementations," *IEEE Trans. Antennas Propag.* **55**(3), 556–567 (2007).
30. Q. Wu, G. D. Feke, R. D. Grober, and L. P. Ghislain, "Realization of numerical aperture 2.0 using a gallium phosphide solid immersion lens," *Appl. Phys. Lett.* **75**(26), 4064–4066 (1999).
31. D. E. Aspnes and A. A. Studna, "Dielectric functions and optical parameters of Si, Ge, GaP, GaAs, GaSb, InP, InAs, and InSb from 1.5 to 6.0 eV," *Phys. Rev. B* **27**(2), 985–1009 (1983).
32. B. D. Terris, H. J. Mamin, D. Rugar, W. R. Studenmund, and G. S. Kino, "Near-field optical data storage using a solid immersion lens," *Appl. Phys. Lett.* **65**(4), 388–390 (1994).
33. J. A. Davis, D. M. Cottrell, J. Campos, M. J. Yzuel, and I. Moreno, "Encoding amplitude information onto phase-only filters," *Appl. Opt.* **38**(23), 5004–5013 (1999).
34. J. Baumgartl, S. Kosmeier, M. Mazilu, E. T. F. Rogers, N. I. Zheludev, and K. Dholakia, "Far field subwavelength focusing using optical eigenmodes," *Appl. Phys. Lett.* **98**(18), 181109 (2011).
35. H. Fukuda, Y. Kobayashi, T. Tawa, and S. Okazaki, "Performance of pupil-filtering stepper-lens system," *Microelectron. Eng.* **27**(1–4), 213–216 (1995).
36. F. X. Canning, "Corrected Fresnel coefficients for lossy materials," in *IEEE International Symposium on Antennas and Propagation (APSURSI)*, Spokane, WA, 3–8 July (2011).

## 1. Introduction

Magnetic hard disk drive (HDD) technology is essential to majority of modern computers. The areal recording density of HDDs already exceeds 500Gb/in<sup>2</sup>, but further increases in density are critical to keep up with storage demand. However, conventional perpendicular magnetic recording (PMR) is constrained by the superparamagnetic limit [1]: that is, as the bits become more closely spaced, the polarization state in one magnetic grain can change the direction of the magnetic moment in the neighbouring bits, thus making the stored information thermally unstable. Heat assisted magnetic recording (HAMR) is one of the leading technologies in development to beat this limit [2]. HAMR uses a magnetic medium with higher thermal stability but such a medium requires stronger magnetic fields for recording. These fields are higher than can be generated by existing thin-film recording transducers, so HAMR also needs an external laser source to locally heat the recording

regions. This temporary increase in temperature reduces the magnetic resistance of the recording material allowing data writing using a lower magnetic field.

Although the magnetic grain in the recording medium for HAMR is generally small (typically less than 10nm) [2], it is still necessary to use a small heat spot because a spot larger than the bit size will heat neighbouring bits and erase the stored information therein. Thus, an areal density of 1Tb/in<sup>2</sup> (the approximate limit of current PMR technology), requires a focal spot smaller than 50nm in diameter. Conventional optical systems cannot produce such a spot: Abbe's diffraction limit states that the spot size can be no smaller than about half the wavelength. In a previously reported proof-of-concept HAMR system, the researchers used a near-field plasmonic transducer to decrease the focal spot size [3]. Using the surface plasmon resonance at an infrared wavelength and resonant coupling between the transducer and recording medium, the local electric field was greatly enhanced. Thus far, a resolution of 70nm and an areal density of 375Tb/m<sup>2</sup> have been experimentally demonstrated [3].

The plasmonic transducer is a near-field technique which presents considerable manufacturing challenges, for example the transducer dimensions and separation from the substrate waveguide must be precisely controlled to ensure a high coupling efficiency. Tapered waveguides used in the near-field scanning optical microscopy have the capability to achieve a resolution of 100nm or better, but their applications are limited due to the dramatic attenuation of light transmitted through the subwavelength aperture: typical optical throughput is of the order of 10<sup>-4</sup>-10<sup>-5</sup> [4]. Other subwavelength focusing methods based on near-field evanescent waves include the superlens [5–7] and nanoscale spherical lenses [8,9], but all these methods require the lens to be in the immediate proximity of object: typically within distances much less than the wavelength. On the other hand, it has already been experimentally demonstrated that far-field sub-diffraction-limit focusing can be achieved using super-oscillatory focusing [10–14]. In this paper, we apply super-oscillatory focusing to HAMR applications. In combination with solid immersion technology, which is commonly used for high-density optical storage [15], a resolution of 50nm becomes readily achievable, better than can be achieved with a conventional lens and solid immersion.

## 2. Super-oscillation for super resolution focusing

The pivotal idea of super-oscillation is that a super-resolution hotspot can be formed beyond the optical near-field by the interference of propagating waves with low-spatial-frequency wavevectors ( $|k| \leq 2\pi n / \lambda$ ) rather than high-spatial-frequency evanescent components ( $|k| > 2\pi n / \lambda$ ), where  $n$  is the refractive index of surrounding medium. These optical super-oscillations were proposed by Berry and Popescu in 2006 [16] and first seen in 2007 [17, 18]. Mathematically this is allowed because band-limited functions are able to oscillate much faster than the highest frequency Fourier components they contain. This allows us to form subwavelength spots far from any lens but the tradeoff is that some of the input energy goes into sidebands around the spot. Subsequently, it was experimentally shown by the Southampton research group that super-oscillation can be used to achieve optical super-resolution focusing and imaging [10,11,19–21]. Recently, they demonstrated an optical microscope with resolution better than  $\lambda/6$  using a binary super-oscillatory lens (SOL), a nanostructured mask composed of a set of concentric rings of different width and diameter that, through precise control of diffracted waves, produces a far-field subwavelength hotspot [12,13]. A similar superoscillation based optical super-microscope has also been demonstrated to be capable of linear, far-field imaging beyond the diffraction limit [22].

To achieve a suitable spot for HAMR, we develop a new generation of solid immersion SOLs. The schematic configuration is illustrated in Fig. 1(a). An incoming laser is focused by the binary SOL into a high refractive index solid immersion layer to form a deep subwavelength focal spot with a long depth of focus (DOF). This optical needle passes through the solid immersion layer/air interface and locally heats the magnetic disk.



The total mask radius is  $r_{\max} = 20\mu\text{m}$  and the smallest ring width is  $\Delta r = 200\text{nm}$ . The target function is defined as  $\exp(-\frac{r^2}{a^2})\exp\left[-\frac{(z-z_f)^{10}}{b^{10}}\right]$ , where  $z_f$  is the focal length,  $a = \frac{FWHM}{2\sqrt{\ln 2}}$ ,  $b = \frac{DOF}{2\sqrt{\ln 2}}$ ,  $FWHM$  is the full-width half maximum of transverse spot size and  $DOF$  is the depth of focus. Subsequently, the optimization process gives the mask design when minimum of the variance between the actual field distribution and target function within the field of view (FOV, defined as the separation between the two nearest sidebands with 10% intensity of the main lobe) is reached. In the calculation, we used a swarm of 100 particles and 500 iterations and arrived at the three different SOL designs shown above. The ONSOL designs for air,  $\text{SiO}_2$  and GaP are different [Figs. 1(b)–1(d)] because we are aiming to get predefined focal position and DOF in different media, and thus a single SOL design doesn't work well for all the three cases. Due to cylindrical symmetry, only the radial distributions of the transmittance are shown. Furthermore, to attain a reasonable FOV, we constrain the solution space by blocking the central area of the mask (radius  $6\mu\text{m}$ ).

### 3. Solid immersion super-oscillatory optical needle

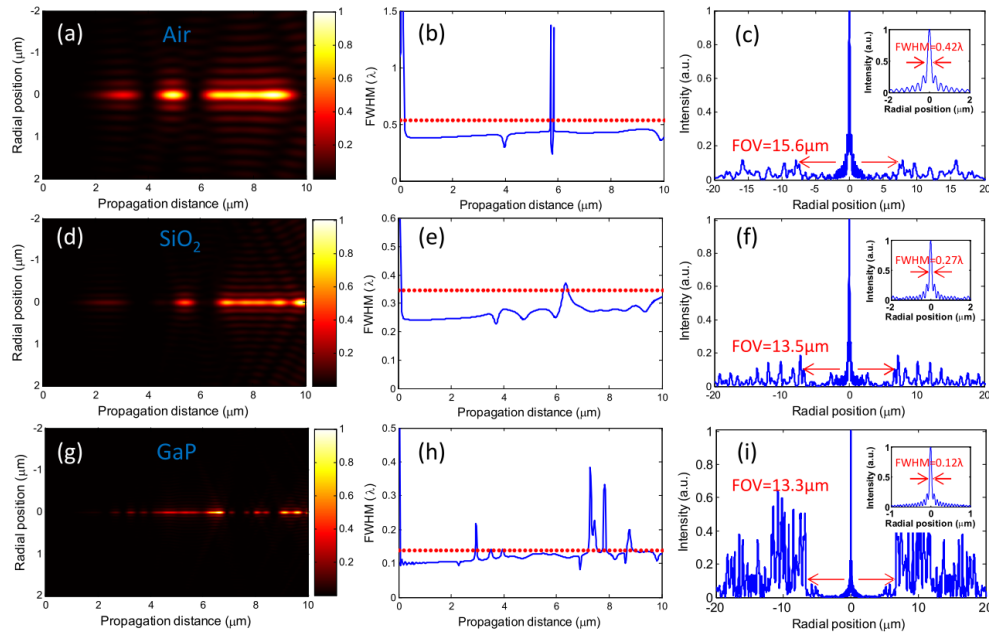


Fig. 2. Generation of super-oscillatory optical needle in air (top row),  $\text{SiO}_2$  (middle row) and GaP (bottom row). (a)(d)(g) Normalized total electric field intensity distribution. (b)(e)(h) Variation of FWHM of light spot with propagation direction (blue lines). The diffraction limit in the corresponding media is plotted (red dotted lines) for comparison. (c)(f)(i) Lineout of electric field intensity distribution along the SOL mask diameter at  $z_f = 8\mu\text{m}$  for air (c) and  $\text{SiO}_2$  (f), and at  $z_f = 5\mu\text{m}$  for GaP (i). Insets in (c)(f)(i) show a close-up of the central main lobe.

We optimized the SOL for use in air with a central focal position and DOF of  $z_f = 8\mu\text{m}$  and  $5\lambda$  respectively. These parameters are chosen in order to comply with the  $6\mu\text{m}$  central opaque region, ensuring a sub-diffraction-limit spot size and reasonable energy concentration in the mainlobe. The optimized design is shown in Fig. 1(b), and the intensity distribution of the resulting needle is shown in Fig. 2(a). The FWHM of the focal spot is shown in Fig. 2(b) as a function of propagation distance and is found to be smaller than  $0.45\lambda$  within the target DOF

(propagation distance from  $6.8\mu\text{m}$  to  $9.2\mu\text{m}$ ,  $\sim 5\lambda$ ). At  $z_f = 8\mu\text{m}$ , the FWHM is  $0.42\lambda$  which is beyond the diffraction limit in air ( $(\lambda / 2n \sin(\theta_{\max})) \approx 0.54\lambda$ , shown as red dotted line in Fig. 2(b)). Here,  $\theta_{\max}$  is the maximal focal angle determined by the mask aperture and focal length through the relation  $\tan(\theta_{\max}) = r_{\max} / z_f$ .

For  $\text{SiO}_2$  ( $n_{\text{SiO}_2} = 1.55061$  at  $\lambda = 473\text{nm}$ ), using the mask in Fig. 1(c), it is obvious that the optical needle becomes sharper while keeping a long DOF along the axial direction [Fig. 2(d)]. In Fig. 2(e) it is shown that, the FWHM is only  $128\text{nm}$  ( $0.27\lambda$ ) at  $z_f = 8\mu\text{m}$ , breaking the diffraction limit in  $\text{SiO}_2$  ( $\sim 0.35\lambda$ ). The total electric field intensity distributions across the mask diameter in air and  $\text{SiO}_2$  at  $z_f = 8\mu\text{m}$  are depicted in Figs. 2(c) and 2(f) respectively. From these two figures, the FOVs in air and  $\text{SiO}_2$  are estimated to be  $15.6\mu\text{m}$  and  $13.5\mu\text{m}$  respectively, which are approximately 33 and 28 times the free space wavelength. Correspondingly, the optical power within the FOVs is 14.4% and 13.7% of the overall transmitted optical power in the two cases, while the peak electric field intensity in the main lobe is still much larger than that of the sidebands.

The focal spot size can be compressed further by using a higher refractive index solid immersion medium such as GaP, which has been used in traditional solid immersion microscopy [30]. Since most of the materials with refractive index larger than 3 at blue wavelengths have large absorption, we must take loss in the medium into account. In this work, the complex refractive index of GaP is taken from [31] to be  $n_{\text{GaP}} = 3.72 + 0.01i$  at our chosen wavelength ( $\lambda = 473\text{nm}$ ), showing a relatively high real part of refractive index and a reasonable imaginary part.

In Fig. 2(g), we show the electric field intensity pattern formed by the ONSOL in the GaP layer. The central focal position and DOF are chosen to be smaller ( $z_f = 5\mu\text{m}$  and  $4\lambda$  respectively) in order to mitigate the absorption loss and achieve a better focusing performance. An optical needle with FWHM of  $57\text{nm}$  ( $\sim 0.12\lambda$  or  $0.45\lambda_{\text{eff}}$ ) is formed near the focal position [Fig. 2(h)] using the mask shown in Fig. 1(d). From the profile of electric field intensity distribution along the mask diameter [Fig. 2(i)], the FOV is seen to be  $13.3\mu\text{m}$ , approximately the same as in air and  $\text{SiO}_2$ . That is to say, the central focal spot is separated from the nearest intense sideband by more than  $13\mu\text{m}$ , allowing the use of opaque aperture or absorbing material to prevent the sidebands hitting the magnetic medium. However, it is noted that the sidebands become more intense in GaP with a peak intensity that is 64% of the main lobe. As a result, the optical power within the FOVs is decreased to 1.8% of the overall optical power in the observation plane at  $z_f = 5\mu\text{m}$ . It should also be noted that, in this case, smaller focal spots can be found at shorter focal lengths, for example the FWHMs at two other foci at  $z = 3.24\mu\text{m}$  and  $z = 2.66\mu\text{m}$  are  $52\text{nm}$  and  $50\text{nm}$  respectively.

To prove the generated focal spots are indeed super-oscillatory, we simulated the local wavevector ( $k_{\text{local}}$ , phase gradient) distributions near the mainlobes in the three cases. The results are presented in Fig. 3. It is clearly seen that the local wavevectors at the minima in the super-oscillation region can be much larger than maximum wavevector ( $k_{\max} = nk_0$ ) in the corresponding media. At the first minimum adjacent to the mainlobe,  $k_{\text{local}}$  are about 21, 18 and 8 times  $k_{\max}$  for the SOL design in air,  $\text{SiO}_2$  and GaP respectively, undoubtedly revealing that the phase oscillates rapidly near the intensity minimum. Therefore, the hot-spot is being squeezed in the super-oscillatory region into a spot smaller than the conventional diffraction limit.

We have shown that super-oscillations can be used to generate super-resolution focal spots with designed axial position, DOF and FWHM, and that high refractive-index immersion media help to reduce the size of focal spot. It is noted that in all cases, the achieved spot size is around  $0.42\lambda_{\text{eff}}$ , where  $\lambda_{\text{eff}} = \lambda / n$  is the effective wavelength in a material with refractive index of  $n$ . The central block is essential to guarantee a reasonable sidelobe-to-mainlobe separation, but in the same time, less electromagnetic energy emanating

from the perforated ring-slits will contribute to the mainlobe at fixed binary mask size. In practice, larger overall mask size with a bigger central block may help to channel more energy in to the mainlobe that is necessary for HAMR operation. The effect of increasing block size for a given overall mask size has been studied in [12]. In this work, 6 $\mu\text{m}$  block radius is a satisfactory choice in terms of FOV, optical needle length and width, and energy content.

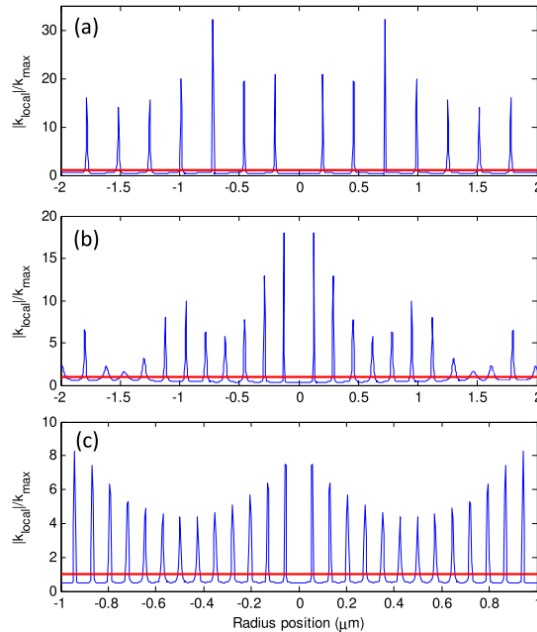


Fig. 3. Local wavevector distributions in the super-oscillatory region: (a) air, (b) SiO<sub>2</sub> and (c) GaP.  $k_{\max} = nk_0$  is the maximum of the band limited wavevectors in the corresponding media. The red lines are at  $k_{\text{local}} = k_{\max}$ .

The super-resolution focusing capability of the SOL mask can be characterized in terms of the effective numerical aperture  $\text{NA}_{\text{eff}}$ . A conventional objective lens can focus the plane wave into a spot with lateral FWHM of  $\lambda/(2\text{NA})$  where NA is the numerical aperture of the objective lens. For our SOL, therefore, we define  $\text{NA}_{\text{eff}} = \lambda/(2 \times \text{FWHM})$ . Using an oil-immersion lens it is possible to achieve an  $\text{NA} \sim 1.4$ , while the possible numerical aperture of a conventional solid immersion lens (SIL) can be as high as 2.0, where the exact value is dependent on the high-refractive-index materials used. However, a SIL does have some drawbacks: a) the numerical aperture is limited by the refractive index of the materials [30]; b) it is required to pre-focus the beam onto the SIL using an additional high objective lens; c) both the hemisphere and Weierstrass sphere [32] commonly used for SILs are three-dimensional structures which are not easy manufacture. It is also difficult to precisely control the sphericity of the SIL which causes aberrations and limits its focusing performance. In comparison, SOL is not limited in the same way and the obtainable  $\text{NA}_{\text{eff}}$  in air, SiO<sub>2</sub> and GaP reported above is 1.19, 1.85 and 4.17 respectively. In addition, the intrinsically flat design of SOL is much easier to integrate with the writing/reading heads for HAMR applications.

It shall be noted that although binary mask are easy to be fabricated and integrated into the HARM head, continuous amplitude and phase masks could achieve even smaller hot-spots. In principle such masks can be generated using liquid crystal spatial light modulators [33, 34] and stepper lens system [35]. Naturally, the simplest way to get the super-oscillatory hot-spot is to let its constituent electromagnetic fields propagate backward to a plane and to construct

the required field distribution by an appropriate continuous amplitude and phase mask. However, it is limited by the manufacturing of super-oscillatory masks with continuously variable phase retardation and optical density. Spatial light modulator can realize both amplitude and phase control, but is still limited by its relatively large pixilation at the level of about  $10\mu\text{m}$  and surface roughness. Therefore, binary mask technology remains the best practical solution [20]. Moreover, it has recently been demonstrated that gradient planar metamaterial arrays can also focus beyond the diffraction limit [11]. On the other hand, reduction of the main lobe spot size is always accompanied by a decrease in the throughput efficiency of the SOL with increasing sideband intensity, which is the intrinsic nature of super-oscillation.

#### 4. Coupling out of solid immersion layer

In a realistic HAMR system, there is always a narrow air gap between the writing head and recording medium to avoid damaging either the head or the medium as the disc rotates [2]. Therefore, we need to understand the performance of optical needle at the solid immersion medium/air interface, and show if the super-oscillatory hot-spot diverges significantly before it reaches the magnetic medium. To do this, we calculate the diffracted field in the plane just before the interface using vectorial diffraction theory (as above), we then take the FFT to get the angular spectrum and apply the Fresnel transmission coefficients for the *s*- and *p*-polarized components in Fourier space. An inverse FFT eventually gives the transmitted field. We note here that the conventional Fresnel coefficients are derived for lossless medium and do not hold for lossy materials. Here we use the corrected equations derived for lossy media [36].

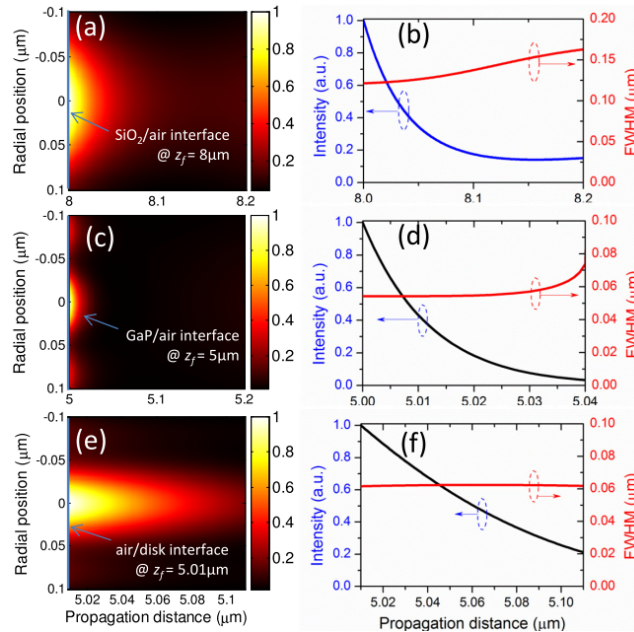


Fig. 4. Performance of super-oscillatory optical needle after solid immersion layer/air interface: (top row)  $\text{SiO}_2/\text{air}$  after  $z_f = 8\mu\text{m}$ , (middle row)  $\text{GaP}/\text{air}$  after  $z_f = 5\mu\text{m}$ , and (bottom row)  $\text{air}/\text{magnetic disk}$  after  $z_f = 5.01\mu\text{m}$ . (a) (c) (e) Normalized total electric field intensity distribution. (b) (d) (f) Electric field intensity (blue line) and FWHM (red line) distribution along the axial direction.

The performance of super-oscillatory optical needle from Fig. 2(d) after the  $\text{SiO}_2/\text{air}$  interface at  $z_f = 8\mu\text{m}$  is shown in Fig. 4 (top row). A detailed analysis of the axial electric field intensity [Fig. 4(b)] indicates that the  $1/e$  intensity penetration depth in air is  $46.5\text{nm}$ . The

FWHM increases from 122nm to 164nm over a propagation distance of 200nm, but remains smaller than 127nm within the penetration depth. This spot size is still well below the diffraction limit in SiO<sub>2</sub> (~166nm). Similarly, the electric field intensity and axial intensity/spot size plots are given in Figs. 4(c) and 4(d) respectively after the GaP/air interface. The penetration depth is evaluated to be 12nm, within which the FWHM keeps almost invariant at 55nm. As might be intuitively expected, the higher the refractive index of the solid immersion medium, the smaller the penetration depth. Although the penetration depth of 12nm seems to be small, the proof-of-concept HAMR system reported in [3] had a physical air gap between the bottom of carbon overcoat of the recording head and the top of the lubricant on the magnetic disk of only ~2nm.

For practical HAMR application, the dielectric properties of the magnetic disk must be considered for accurate calculation of the area of disc heated by the spot. For this purpose, we have studied the optical properties of commercial hard disk drive platter using ellipsometry method. At wavelength of 473nm, its complex refractive index is found to be  $4.71 + 0.455i$ . Using this data and SOL design in Fig. 1(d), we have calculated the electric field intensity distributions in the recording layer where 10nm air gap was assumed between the Gap layer and magnetic disk surface. Through detailed analysis, the achievable spot size in the magnetic recording layer is evaluated to be ~62nm within the penetration depth of 60nm, inferred from the total electric field intensity distribution and line-scan profile shown in Figs. 4(e) and 4(f) respectively. This spot size is comparable with that reported in [3], which seems to be the most promising HAMR technology in industry at present.

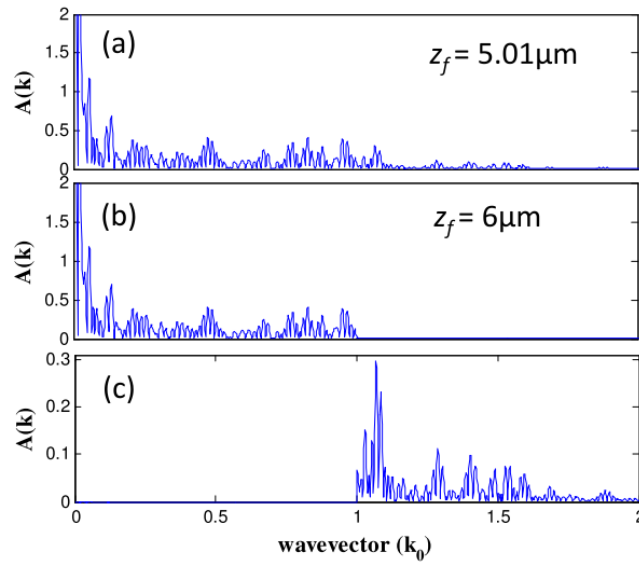


Fig. 5. Angular spectrum of super-oscillatory spot after GaP/air interface: (a) at  $z_f = 5.01\mu\text{m}$  and (b) at  $z_f = 6\mu\text{m}$ . Their subtraction is given in (c), which clearly indicates the super-oscillatory spot after the interface is originating from the evanescent components within wavevector ranges  $[-nk_0, -k_0]$  and  $[k_0, nk_0]$ .

As studied by Berry in [16], the super-oscillatory fields are able to propagate into the far-field without evanescent components. This is true in the solid-immersion medium where only propagating mode contributes to the super-oscillatory spot. However after the GaP/air interface, only the near-field wavevectors remain due to discontinuity in the refractive index. Here the GaP/air interface acts as a spatial frequency filter to change the band limited wavevector range from  $[-nk_0, nk_0]$  to  $[-k_0, k_0]$  when the light propagates into the far-field in the air side, where  $k_0$  is the wavevector of light in air and  $n$  is the real part of refractive

index of GaP. The diffraction fields from the binary mask with larger incident angle than the critical angle ( $\sim 15.6^\circ$ ) will totally disappear after a certain distance. In order to precisely elaborate that the super-oscillatory focal spots after the GaP/air interface are originating from the evanescent components, we have calculated the Fourier components of the transmitted fields both in the near-field region (10nm after the interface) and far-field region ( $1\mu\text{m}$  after the interface). The results are given in Figs. 5(a) and 5(b) respectively. It is obviously seen that the wavevector larger than  $k_0$  was cut off in the far-field angular spectra, while remained in the near-field region (only the positive spectra are shown here due to symmetry). By subtraction of the angular spectrum components in Fig. 5(b) from Fig. 5(a), we can infer the contribution from the evanescent components, as shown in Fig. 5(c). Therefore, we can conclude that the super-oscillatory focal spots are indeed coming from the evanescent modes and the overall electric field after the interface will exponentially decay.

## 5. Conclusions

In summary, we have demonstrated a solid-immersion super-oscillatory lens for heat-assisted magnetic recording capable of producing a sub-50nm hot-spots using a diode laser with wavelength of  $\lambda = 473$  nm and effective numerical aperture of 4.17. The super-oscillatory mask is optimized using a binary particle swarm optimization algorithm and the diffracted fields are calculated using the vectorial angular spectrum method. Super-resolved optical needles with depth of focus of several wavelengths were successfully generated in air, and  $\text{SiO}_2$  and GaP immersion layers delivering hot-spots of  $0.42\lambda$ ,  $0.27\lambda$  and  $0.12\lambda$  respectively, corresponding to an effective numerical aperture of 1.19, 1.85 and 4.17. By using an SOL with an opaque central region, the field of view is increased to  $\sim 13\mu\text{m}$ , leading to practical HAMR applications. The coupling of super-oscillatory optical needle out of the solid immersion medium and into the magnetic recording layer is studied, while the intensity on the air side is shown to be exponentially decaying, the sub-diffraction limit spot size is maintained.

## Acknowledgments

The work is partially supported by the Advanced Optics in Engineering Programme from the Agency for Science, Technology and Research (A\*STAR) of Singapore with Grant number 122-360-0009 and the UK Engineering and Physical Sciences Research Council with Grant numbers EP/F040644/1 and EP/G060363/1, the Royal Society of London, and the University of Southampton Enterprise Fund.